METHODS

Trajectum framework and Bayesian analysis. The *Trajectum* framework used in this study contains four successive components: an initial-state construction, followed by pre-equilibrium dynamics, a hydrodynamic evolution stage, and a conversion to hadrons followed by hadronic transport with SMASH [1, 2]. Here, we briefly summarize the parameters entering the calculation, the observables used to constrain them, and the statistical procedure employed. More extensive technical details are given in Ref. [3].

In the initial stage, nucleons are sampled inside the colliding nuclei according to Eq. (3) of the main text, where for ^{208}Pb we use separate parameters for protons and neutrons, and where for ^{129}Xe we use a single description for both. In addition, the surface of the density is deformed via

$$R(\theta) = R\big(1 + \beta_2 \cos\gamma Y_2^0(\theta) + \beta_2 \sin\gamma Y_2^2(\theta) + \beta_3 Y_3^0(\theta)\big), \tag{1}$$

where R is the half-width radius, β_2 measures the quadrupole deformation, γ measures the triaxiality, and β_3 measures the octupole deformation. For ^{208}Pb, $\gamma = 0$ and we let β_2 and β_3 fluctuate around zero according to a Gaussian distribution with width

$$\sigma(\beta_n) \equiv \sqrt{\langle \beta_n^2 \rangle}. \tag{2}$$

In this work we do not enforce a short-range repulsion among nucleons (often done by a minimum nucleon-nucleon separation), mostly since the current implementation does not support such a minimum distance for triaxial nuclei. The colliding nucleons (referred to as participants) are selected using the measured inelastic cross section $\sigma_{\rm NN}$, following Ref. [4].

Each participant is represented as n_c constituents, each carrying a transverse Gaussian profile of width

$$v = 0.2 \text{ fm} + \chi_{\rm struct}\,(w - 0.2 \text{ fm}). \tag{3}$$

The constituent centers are themselves Gaussian distributed, so that the average nucleon profile has width w. Summing over participants and their constituents yields the thickness functions $\mathcal{T}_{A/B}$. The normalization of each constituent fluctuates as $N\gamma/n_c$, where γ is drawn from a gamma distribution with mean unity and width $\sigma_{\rm fluct}\sqrt{n_c}$, where N and $\sigma_{\rm fluct}$ are parameters. The initial energy density e is then obtained from the thickness functions by the T$_{\rm R}$ENTo formula

$$\tau e|_{\tau\to 0^+} \propto \left(\frac{\mathcal{T}_A^p + \mathcal{T}_B^p}{2}\right)^{q/p},$$

with parameters p and q.

During a time interval $\tau_{\rm hyd}$, this initial energy density is evolved in two ways: by free streaming, and by a holographically motivated prescription [5]. These results are interpolated between these two limits using a continuous parameter $r_{\rm hyd}$, with $r_{\rm hyd} = 0$ corresponding to free streaming and $r_{\rm hyd} = 1$ to the holographic choice. This interpolation is then used to initialize the hydrodynamic simulation.

The stress-energy tensor is then propagated with second-order viscous hydrodynamics. Nine parameters control the transport sector: $(\eta/s)_{\rm ave}$, $(\eta/s)_{\rm slope}$, $(\eta/s)_{\delta\rm slope}$, $(\eta/s)_{0.8\,\rm GeV}$, $(\zeta/s)_{\rm max}$, $(\zeta/s)_{m\times w}$, $(\zeta/s)_{T_0}$, $\tau_\pi sT/\eta$, and $\tau_{\pi\pi}/\tau_\pi$. The first four specify the temperature dependence of the shear-viscosity-to-entropy ratio, namely its mean value, its slope between 150 and 300 MeV, the change in slope at higher temperature, and its value at 800 MeV and above. The next three parameters determine the peak of the bulk viscosity, its effective width times height, and the temperature at which that peak is centered. The last two are dimensionless second-order combinations; in particular, $\tau_\pi sT/\eta$ controls the relaxation toward first-order viscous hydrodynamics. In this work we keep the equation-of-state coming from the HotQCD lattice computations fixed, as described in the original works by [6–8].

At the switching temperature $T_{\rm switch}$, the fluid is converted to hadrons using the Cooper-Frye prescription with Pratt-Torrieri-Bernhard viscous corrections [7, 9]. The resulting hadrons are subsequently evolved in SMASH, where all hadronic cross sections are multiplied by a factor $f_{\rm SMASH}$.

A final normalization parameter, cent$_{\rm norm}$, adjusts the anchor point of the centrality (defining which multiplicity corresponds to 100% centrality). This is the only parameter assigned a non-flat prior; it is taken to follow a Gaussian prior with a width of 1% around 100%.

To focus on a robust determination of the shape of ^{129}Xe this analysis uses a broad range of p_T-integrated observables for both ^{208}Pb, ^{129}Xe and importantly their ratio where possible. This includes the total hadronic cross sections in ^{208}Pb+^{208}Pb collisions [10], identified and unidentified yields $dN_{\rm ch}/dy$ and mean transverse momenta $\langle p_T\rangle$ for pions, kaons, protons and charged hadrons respectively [11, 12]. For xenon we similarly take the unidentified yields from [13]. Since this comes from the same experiment we model a mild cancellation of the uncertainty in the ratio by assuming the uncertainties are given by the maximum uncertainty instead of the quadratic sum. Integrated anisotropic flow coefficients for Pb-Pb and Xe-Xe collisions are given in respectively [14] and [15].

All these observables were from the ALICE collaboration, but subsequently we take the $\langle p_T\rangle$ fluctuations and the $\rho_2(v_2\{2\}^2, \langle p_T\rangle)$ correlator for both Xe-Xe and Pb-Pb from the ATLAS collaboration [16].

The posterior distribution is then evaluated using Bayes' theorem,

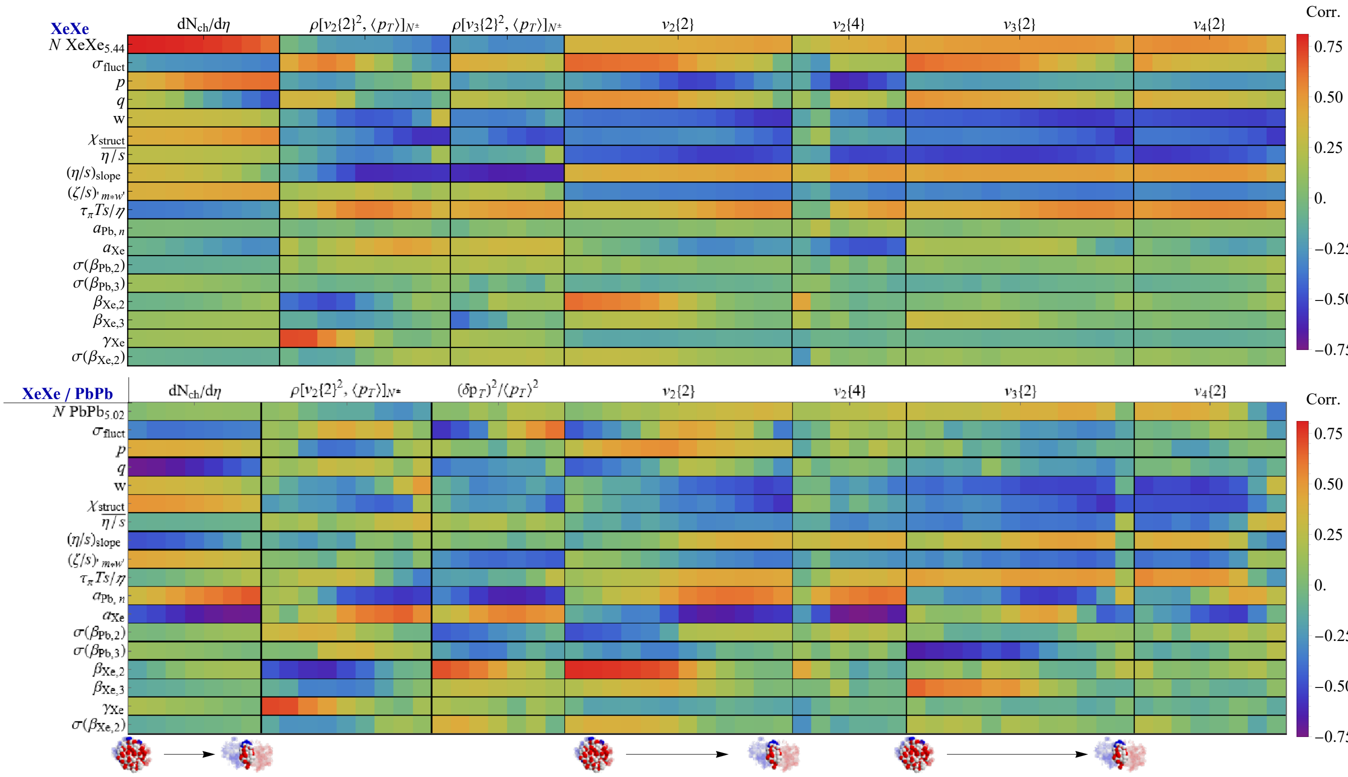

FIG. 1. **Full sensitivity matrix of observables against model parameters.** We present Xe-Xe collisions (top) and Xe-Xe relative to Pb-Pb collisions (bottom). We display ^{208}Pb structure parameters in the upper panel to show they do not affect the Xe-Xe observables.

$$P(x \mid y_{\rm exp}) = \frac{e^{-\Delta^2/2}}{\sqrt{(2\pi)^n \det \Sigma(x)}} P(x), \tag{4}$$

with a flat prior $P(x)$ for all parameters except $\text{cent}_{\text{norm}}$. The quadratic form entering the likelihood is

$$\Delta^2 = \big(y(x) - y_{\rm exp}\big) \cdot \Sigma(x)^{-1} \cdot \big(y(x) - y_{\rm exp}\big), \tag{5}$$

where $y(x)$ denotes the model prediction, $y_{\rm exp}$ the experimental data vector with n entries, and $\Sigma(x)$ the sum of theoretical and experimental covariance matrices. Those covariance matrices are built as in Ref. [7].

The standard workflow is to evaluate the model on a Latin-hypercube design and then train an emulator for $y(x)$, which is subsequently sampled with the parallel-tempered `emcee` code [17, 18]. In the present analysis, 750 design points were used. At each design point, one million initial conditions were generated; among these, 40×10^3 events were evolved hydrodynamically; and roughly 200×10^3 SMASH events were produced to maintain sufficient statistics even for 0-1% collisions (*Trajectum* was initially set up such that these collisions are sampled preferentially [3]).

As explained in [5] it is often important to critically assess the full uncertainty matrix. This includes in particular theoretical uncertainties associated with imperfect modeling, which was in a simplified way taking into account by 'observable weighting'. Here we perhaps go for an even simpler option by setting all uncertainties at a minimum value of 4%. This avoids overfitting the data and we will come back shortly to its effects.

Full correlation matrix and results. In Fig. 1 we present the same sensitivity matrix shown in Fig. 2 of the main text, including now the full list of model parameters varied in the analysis, as well as absolute values of observables in Xe-Xe collisions (upper panel). We stress once more the effectiveness of looking at relative quantities to suppress effects related to QGP medium properties. Such a possibility has been argued and documented repeatedly in the literature [19–24], and is demonstrated here for the first time in a fully systematic calculation.

In Fig. 2, we provide the corner plot displaying the correlations among all model parameters as well as the corresponding posterior distributions. Prior ranges and Maximum a Posteriori (MAP) values for the fitted parameters are listed in Tab. I.

In Fig. 3 we show comparisons between our model and all other observables that were employed in the Bayesian fit and that have not been shown in the main text.

Assessing robustness of results. We want to assess how our results change under two variations of the Bayesian analysis, namely,

- by fitting experimental measurements with original

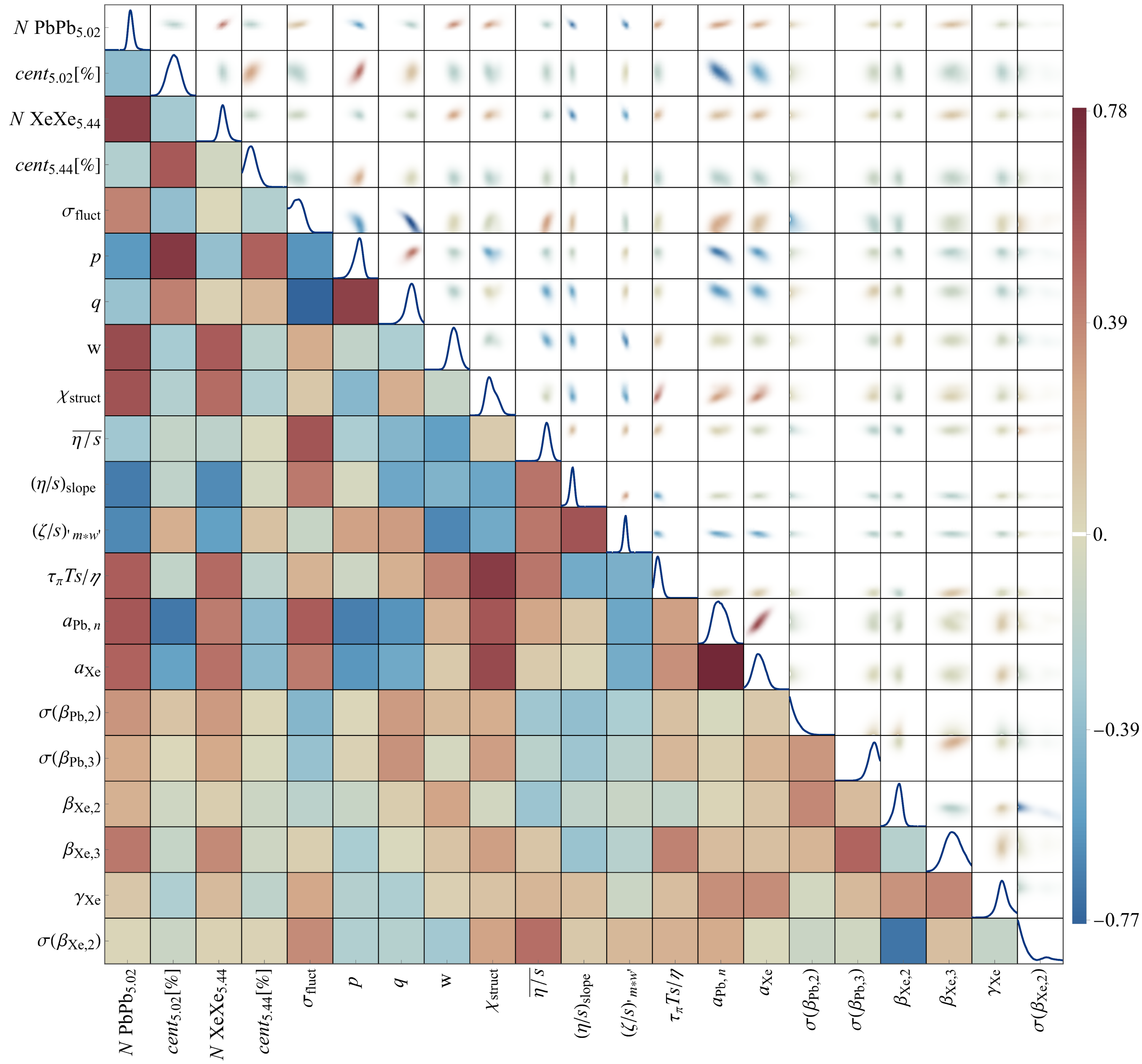

FIG. 2. **Full posterior correlation matrix in the parameter space.** Prior ranges are provided in Tab. I.

uncertainties, rather than inflated to a minimum of 4% relative errors;

- by adding to the fit parameters the half-width radius of the neutron distribution of ^{208}Pb (while keeping 4% errors on the experimental results).

For completeness, for ^{208}Pb we split the Woods-Saxon density into a proton density and a neutron density,

$$\rho^{\rm WS}_{n,p} \propto \left(1 + \frac{r - R(R_{n,p};\theta,\phi)}{a_{n,p}}\right)^{-1}, \qquad (6)$$

where the spherical harmonic expansion of R carries the same parameters β_n and γ for both protons and neutrons. For ^{208}Pb, our default choices are $a_p = 0.448$ fm and $R_p = 6.68$ fm, which are constrained by electron scattering experiments at low energy [25]. For the neutron half-width radius, our standard choice is $R_n = 6.80$ fm, i.e., we implement a shift of 0.12 fm with respect to R_p, as suggested by mean-field calculations [26]. The value of a_n for ^{208}Pb is instead a fit parameter. From such an estimate, then, we can evaluate the rms point-proton and point-neutron radii, and estimate the neutron skin Δr_{np} of ^{208}Pb. For ^{129}Xe, we implement identical proton and neutron distributions and only attempt at extract-

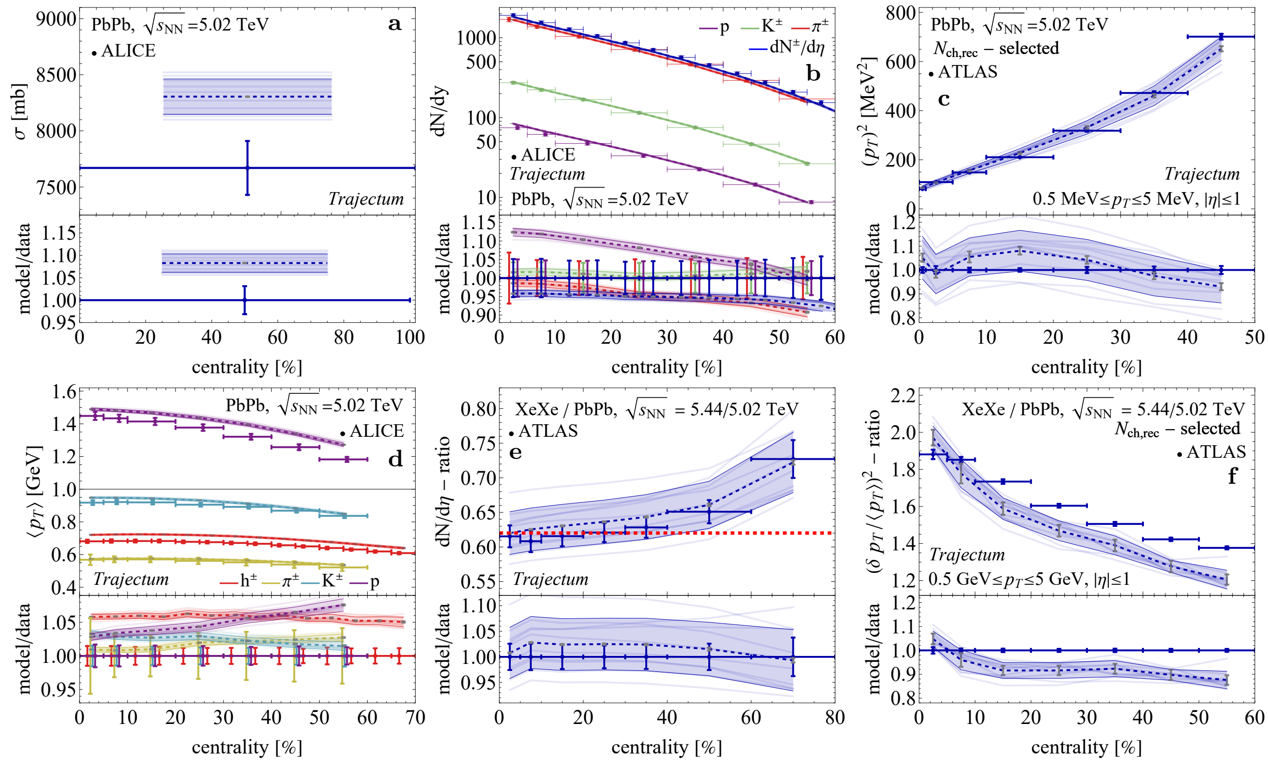

FIG. 3. **Fitted observables.** We show model results for all observables used in the Bayesian fit that were not highlighted in Fig. 3 of the main text. The red dashed line in panel **e** corresponds to the ratio of mass numbers, 129/208, indicating that the multiplicity nicely scales with the number of colliding nucleons.

ing an overall diffuseness parameter $a_{\rm Xe}$, while keeping $R_{\rm Xe} = 5.60$ fm, given by mean-field results [27]. With this setup, we obtain the posterior distributions of $a_{{\rm Pb},n}$ and $a_{\rm Xe}$ shown in Fig. 2.

The results for relevant posterior distributions of parameters are shown in Fig. 4. Results for our standard setup are shown as red solid lines.

Considering true experimental uncertainties in the fit, we obtain the posterior distributions depicted as purple dotted lines. Our first observation is that the determination of the deformation parameters introduced for ^{129}Xe and ^{208}Pb in Figs. 4d-i are essentially unchanged compared to the default fit. The determination of the neutron skin of ^{208}Pb is then in Fig. 4c. It is consistent with our previous determination [28], and is also only marginally affected by the lifting of a minimal experimental uncertainty. Dramatic changes are instead observed for the posterior distributions of parameters that model the structure of colliding nucleons, namely, the nucleon size, w, and the constituent size, $\chi_{\rm struct}$ (where we set three constituents per nucleon). The nucleon size appears to suffer from the well-documented problem of favoring unreasonably large values in the posterior [29, 30]. Remarkably, though, the posterior distribution of the nucleon constituent size, $\chi_{\rm struct}$, exhibits a well-defined peak, substantially improving our previous determination [28]. Likely, this is because our fits now contain the $\rho(v_n\{2\}^2, \langle p_T\rangle)$ observables, that in off-central collisions are sensitive to the granularity of the initial states [31].

Now, we promote R_n to a fit parameter, while keeping relative experimental errors to a minimum of 4%. Again, our first remark is that this yields almost no change in the posterior distributions of the deformation parameters in Fig. 4d-i. Similarly, the nucleon structure parameters are only marginally affected in panels a-b. However, the fit returns an unreasonably small value of the half-width radius, $R_n \approx 5.50$ fm, lower than the proton R_p value and inconsistent with the mean-field results.

Inspecting the sensitivity of observables to R_n, this seems to be mostly driven by the total hadronic cross section, which naturally depends on the nuclear size, and which seems to be pushing R_n to small values (see e.g. Fig. 3). While this requires further clarification, the crucial consequence is a shift in the neutron skin toward zero. Indeed, with this change the posterior distribution of the skin is essentially consistent with zero in Fig. 4c. It would be of great help to find observables offering a dedicated sensibility to R_n in ^{208}Pb. One possibility may come from electroweak boson production in peripheral Pb-Pb collisions, which is sensitive to neutron distributions [32]. The rapidity dependence of baryon stopping has also emerged as a potential sensitive probe of the neutron skin [33–35].

TABLE I. **List of parameter values resulting from the fit of LHC data.** Prior ranges (Lower, Upper) and maximum *a posteriori* (MAP) estimates for the model parameters obtained from the Bayesian calibration to Pb–Pb collisions at $\sqrt{s_{NN}} = 5.02$ TeV and Xe–Xe collisions at $\sqrt{s_{NN}} = 5.44$ TeV. Parameters are grouped by collision-system normalizations, initial-state, nuclear structure, and QGP transport properties. The bottom block lists parameters held fixed in the present analysis; their values are taken from the MAP estimates of a previous Bayesian calibration at $\sqrt{s_{NN}} = 2.76$ and 5.02 TeV [28].

Parameter	Lower	Upper	MAP
Collision-system normalizations			
Norm [5.02 TeV] (GeV)	14	30	23.8
$\mathrm{cent}_{\max}$ [5.02 TeV] (%)	97	103	99.3
Norm [5.44 TeV] (GeV)	14	30	23.5
$\mathrm{cent}_{\max}$ [5.44 TeV] (%)	97	103	97.1
Initial state (TRENTo)			
σ_{fluct}	0.1	1	0.399
p	-0.4	0.4	-0.0498
q	1	1.45	1.28
w (fm)	0.4	0.8	0.700
χ_{struct}	0	1	0.428
Nuclear structure			
$a_{\mathrm{Pb},n}$ (fm)	0.45	0.7	0.599
$\sigma(\beta_{\mathrm{Pb},2})$	0	0.15	0.0088
$\sigma(\beta_{\mathrm{Pb},3})$	0	0.15	0.127
a_{Xe} (fm)	0.45	0.7	0.549
$\beta_{\mathrm{Xe},2}$	0.1	0.3	0.194
$\beta_{\mathrm{Xe},3}$	0	0.15	0.0858
γ_{Xe} (deg)	0	60	40.8
$\sigma(\beta_{\mathrm{Xe},2})$	0	0.2	0.00545
QGP transport			
$(\eta/s)_{\mathrm{ave}}$	0.1	0.25	0.202
$(\eta/s)_{\mathrm{slope}}$ (GeV^{-1})	-1	2	-0.261
$(\zeta/s)_{\max\times\mathrm{width}}$ (GeV)	0	0.02	0.00721
$\tau_\pi\, sT/\eta$	1	10	1.83
Fixed parameters, mostly taken from [28]			
σ_{NN} [5.02 TeV] (mb)	—	—	67.6
σ_{NN} [5.44 TeV] (mb)	—	—	68.5
$d_{\min}$ (fm)	—	—	0
$R_{\mathrm{Pb},n}$ (fm)	—	—	6.80
n_c	—	—	2.88
τ_{hyd} (fm/c)	—	—	0.397
$(\eta/s)_{\delta\mathrm{slope}}$ (GeV^{-1})	—	—	-0.393
$(\eta/s)_{0.8\,\mathrm{GeV}}$	—	—	0.344
$(\zeta/s)_{\max}$	—	—	0.072
$(\zeta/s)_{T_0}$ (GeV)	—	—	0.440
$\tau_{\pi\pi}/\tau_\pi$	—	—	2.52
r_{hyd}	—	—	0.798
T_{switch} (MeV)	—	—	154
a_{EOS}	—	—	-8.7704
f_{SMASH}	—	—	0.953

Event selection effects on $\rho(v_2\{2\}^2, \langle p_T\rangle)$***.*** In this part, several subtleties in computing the $\rho(v_2\{2\}^2, \langle p_T\rangle)$ correlator are discussed. First, it is important to realize that the correlator depends sensitively on exactly which events are used to evaluate it. This is always done in small centrality classes (standard 1% in *Trajectum*, typically one or a few particles experimentally). Then it is important how exactly centrality is defined. For the ATLAS analysis, this is typically done using the forward calorimeter (forward E_T-selected) or using mid-rapidity tracks (mid-rapidity $N_{\mathrm{ch,rec}}$-selected). While the particles used in computing the correlator itself are always corrected for detector effects, this is typically not done when using the centrality selection.

An advantage of the forward centrality estimator is that there is no self-correlation with the measurement area at mid-rapidity and hence this estimator is often preferred by experiments. For *Trajectum*, however, this poses a problem, since it is a boost invariant code that is optimized at mid-rapidity. Luckily, the ATLAS collaboration in the auxiliary figures [16], provided results for both centrality estimators.

Fig. 5 (a) provides ATLAS and *Trajectum* results for both centrality estimators and for *Trajectum* an extra mid-rapidity centrality estimator that differs by the lower p_T cut for the charged hadrons (0.3 GeV as opposed to the standard 0.5 GeV). Somewhat interestingly, we see that the ATLAS correlator depends strongly on $N_{\mathrm{ch,rec}}$-mid-rapidity versus E_T-forward for the central bins, while for *Trajectum* we see a strong difference for peripheral bins (compare the red curves versus the green curves). The combination means that the model misses the data by an almost constant off-set of about 0.05. We also see that for $N_{\mathrm{ch,rec}}$-mid-rapidity the lower p_T cut is important for peripheral bins (purple versus red).

Figure 5 (left) uses parameters that are fitted to the $N_{\mathrm{ch,rec}}$-mid-rapidity with $|\eta| < 1.0$ cut, so it is not surprising that this fits best. It is hence a sensible question if we can fit the E_T-forward selection, and also if we can fit while using the (ATLAS preferred) cut of $|\eta| < 2.5$. This is explored in Fig. 5 (b, c), respectively, for the η cut and the E_T-forward selection. Perhaps curiously refitting the parameters does not bring the model much closer to the $|\eta| < 2.5$ ATLAS results (this data is significantly higher than the $|\eta| < 1.0$ cut). Since the *Trajectum* model is fully calibrated at mid-rapidity (with most data in the range $|\eta| < 0.8$) it is not surprising that *Trajectum* performs better in the narrower range, but it is still interesting that a refit cannot get the correlator to move much closer to the data. Instead, in Fig. 5 (c) we see that this is in fact possible for the E_T-forward selection. Nevertheless, for *Trajectum* the most realistic apples-to-apples comparison is at the mid-rapidity region since this is where the model works optimally.

Lastly, in Fig. 6 we present a simple estimate of the difference in using $N_{\mathrm{ch,\,rec}}$ (as ATLAS does) versus fully de-

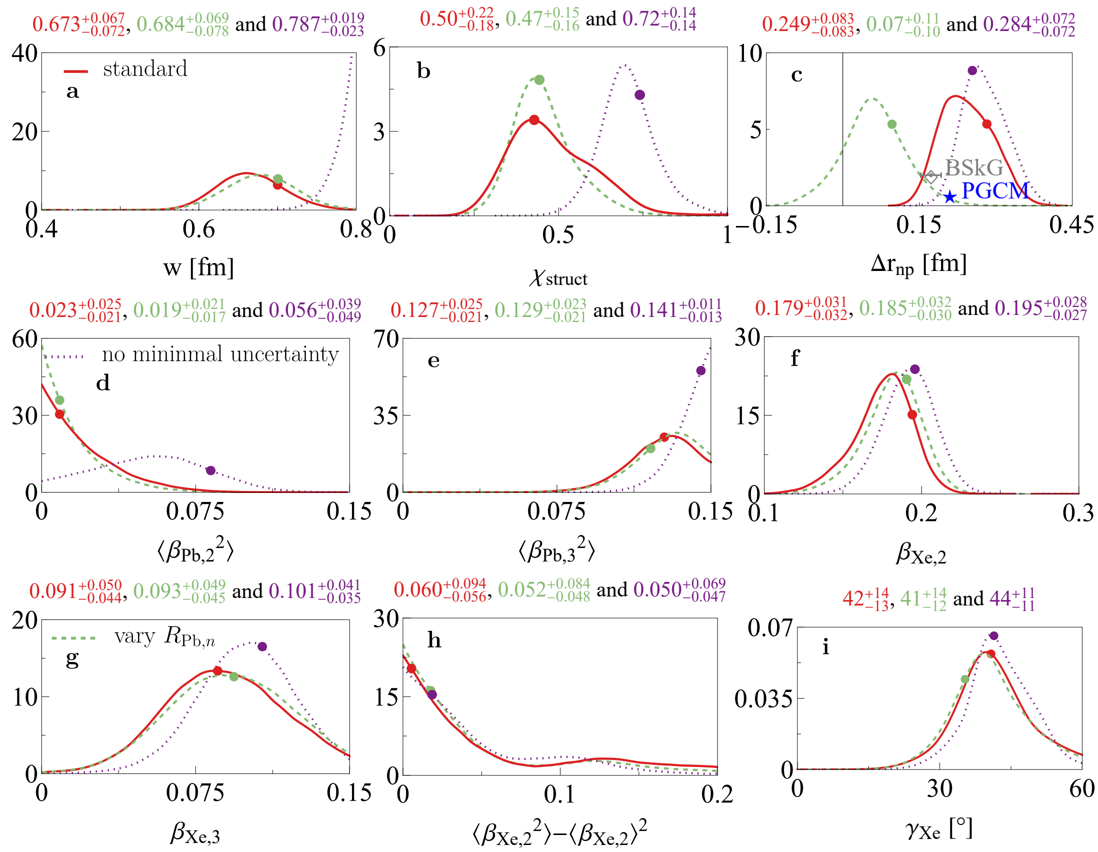

FIG. 4. **Posterior distributions of key initial-state parameters**. They result from three different iterations of the global Bayesian analysis of LHC data. **a-b**: nucleon structure parameters. **c**: neutron skin of lead, including the PGCM value of 0.21 fm, and the BSkG1-5 value of 0.173 ± 0.020 fm. **d-e**: standard deviation of quadrupole and octupole deformation parameters in lead. **f-i**: axial and triaxial deformations in ^{129}Xe. The dots represent the MAP values of the inferred parameters (see Tab. I), also reported on top of each panel. Solid lines: Default setup, as discussed in the main text. Dotted line: fitting experimental data with original error. Dashed lines: fitting experimental data with a minimum 4% relative error and including the half-width radius of ^{208}Pb, R_n, in the fit.

tector corrected charged hadrons. This is somewhat difficult to estimate, so here we suffice by assuming a 67% efficiency that linearly increases to 100% from $0.5-2.5$ GeV. We see that the result is small (barely larger than the *Trajectum* systematic uncertainty), but note that when comparing with the standard centrality selection in this example we find a difference that is for peripheral bins slightly larger than the ATLAS systematic uncertainty.

All effects studied in this part are, of course, relatively small. Nevertheless, since we aim to obtain an accurate estimate of the shape of ^{129}Xe, it is important to ensure that model-to-data comparisons are meaningful, allowing us to report reliable theoretical systematic uncertainties. It is for this reason that in the main text we use the mid-rapidity centrality selector with a narrow rapidity range, which is perhaps unconventional (not the "preferred" experimental choice). We stress that the analysis here really benefited from the wide scale of experimental results available from [16].

Evidence of octupole-deformed shapes. Our fits also include octupole deformation parameters, β_3, for the colliding nuclei. We follow two different implementations for the two nuclei under consideration.

- For ^{129}Xe, we implement a value of $\beta_{\rm Xe,3}$ that is the same for all nuclei and that we fit from the data.
- For ^{208}Pb, we instead sample for each simulated nucleus a value of β_3 from a Gaussian distribution centered at zero and with standard deviation $\sigma(\beta_{\rm Pb,3})$, which we also fit from the data.

Quite interestingly, while fluctuations of the quadrupole parameters, $\sigma(\beta_2)$, turn out to be almost negligible for both nuclei, the lead octupole deformation fluctuation is significant and of order $\sigma(\beta_{\rm Pb,3}) \approx 0.1$. The posterior distributions are shown in Fig. 2, while MAP values are given in Tab. I.

This result seemingly validates recent claims that the inclusion of an octupole deformation parameter in the

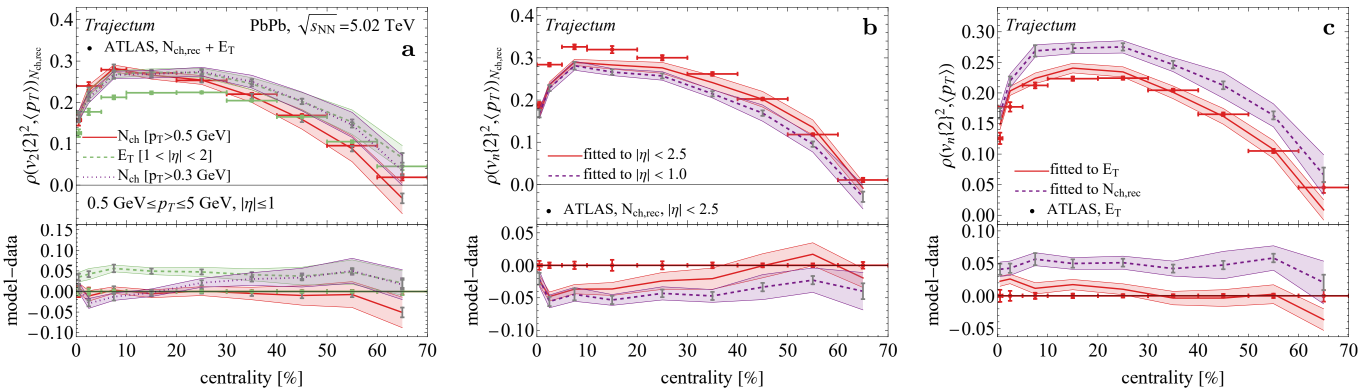

FIG. 5. **Systematic bias on the computation of** $\rho(v_2\{2\}^2, \langle p_T\rangle)$. **a** We show the $\rho(v_2\{2\}^2, \langle p_T\rangle)$ correlator for several centrality selections, both experimentally and from the model. Panels **b** and **c** explore a refit of the parameters fitting instead to a larger rapidity range (**b**) or the forward calorimetric centrality estimator (**c**). Note that the *Trajectum* evaluation of the observable is modified accordingly, but that we still see that only in (**c**) a satisfactory fit is possible.

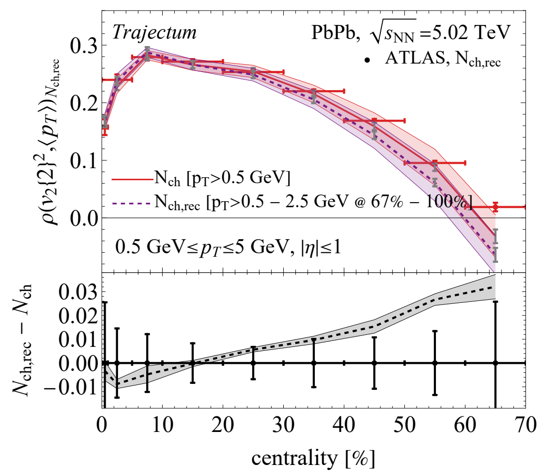

FIG. 6. **Rough estimate of the detector effects present in** $\rho(v_2\{2\}^2, \langle p_T\rangle)$**.** We assess the effect of using tracks instead of detector-corrected charged hadrons for the mid-rapidity centrality selection. It is a simple estimate (see text for details), but the effect in peripheral bins is of the same order as the systematic uncertainty.

modeling of ^{208}Pb improves the description of the rms triangular flow coefficient, $v_3\{2\}$, in central collisions [36, 37]. Quantitative conclusions can be greatly improved in the future by studying the fourth-order cumulant of the triangular flow, $v_3\{4\}$, which is highly sensitive to shape fluctuations [37, 38]. A detailed Bayesian study of the fourth-order cumulant of the v_3 distribution is currently beyond our possibilities. Recent advances with neural networks are promising in this respect [39].

Leading-order estimate of the $v_2\{2\}$ ***ratio.*** We now provide a leading-order estimate of the ratio of elliptic flow coefficients between ultra-central ^{129}Xe + ^{129}Xe and ^{208}Pb + ^{208}Pb collisions that helps clarify how such an observable is linked to the expectation value of the two-body angular correlation of Eq. (7) of the main text.

To start, we assume a linear hydrodynamic response between the rms initial ellipticity of the QGP and the final rms elliptic flow,

$$v_2\{2\} = \kappa_2\, \varepsilon_2\{2\}. \tag{7}$$

Here κ_2 is the linear hydrodynamic response coefficient, while ε_2 is the second-order eccentricity of the QGP entropy density at the beginning of the hydrodynamic expansion. The previous relation implies, in particular,

$$\frac{v_2\{2\}_{\rm XeXe}}{v_2\{2\}_{\rm PbPb}} = \frac{\kappa_{2,\rm XeXe}}{\kappa_{2,\rm PbPb}} \frac{\varepsilon_2\{2\}_{\rm XeXe}}{\varepsilon_2\{2\}_{\rm PbPb}}. \tag{8}$$

Now, we consider collisions at zero impact parameter in which all nucleons in the colliding ions participate in the interaction. Further, we consider that the total entropy of the QGP is directly proportional to the mass number of the colliding nuclei, which is consistent with both data and comprehensive model-to-data comparisons [5]. Under such conditions, for $A \gg 1$ and to leading-order in the fluctuation of the entropy density field, the mean-squared elliptic flow reads [40, 41]

$$v_2\{2\}^2 = \frac{\kappa_2^2}{2A}\left[\frac{\langle R_4\rangle_1}{\langle R_2\rangle_1^2} + A\frac{\langle \mathcal{E}_2\,\mathcal{E}_{-2}\rangle_2}{\langle R_2\rangle_1^2}\right], \tag{9}$$

where quantum expectation values are taken following the same convention of the main text, that is

$$\langle \mathcal{O}\rangle_n = \int d\mathbf{r}_1\cdots d\mathbf{r}_n\, \rho^{(n)}(\mathbf{r}_1\ldots\mathbf{r}_n)\mathcal{O}(\mathbf{r}_1\ldots\mathbf{r}_n), \tag{10}$$

with the following normalization for the many-body densities

$$\int d\mathbf{r}_1 d\mathbf{r}_2\, \rho^{(2)}(\mathbf{r}_1, \mathbf{r}_2) = \int d\mathbf{r}\, \rho^{(1)}(\mathbf{r}) = 1\,. \tag{11}$$

From the hydrodynamic calculations, in the ultra-central

		^{208}Pb	^{129}Xe
1-body	$\langle R_2\rangle_1$ [fm^2]	$20.92(14)_{\rm syst}$	$15.47(42)_{\rm syst}$
	$\langle R_3\rangle_1$ [fm^3]	$115.0(13)_{\rm syst}$	$74.0(33)_{\rm syst}$
	$\langle R_4\rangle_1$ [fm^4]	$681(12)_{\rm syst}$	$384(26)_{\rm syst}$
	$\langle R_6\rangle_1$ [fm^6]	$28.4(9)_{\rm syst}\times 10^3$	$12.6(15)_{\rm syst}\times 10^3$
2-body	$\langle \mathcal{E}_2\,\mathcal{E}_{-2}\rangle_2/\langle R_2\rangle_1^2$	$0.29(3)_{\rm stat}(56)_{\rm syst}\times 10^{-3}$	$13.1(1)_{\rm stat}(19)_{\rm syst}\times 10^{-3}$
	$\langle \mathcal{E}_3\,\mathcal{E}_{-3}\rangle_2/\langle R_3\rangle_1^2$	$-29(38)_{\rm stat}\times 10^{-6}$	$4.3(1)_{\rm stat}(26)_{\rm syst}\times 10^{-3}$
3-body	$(\ \langle R_2\,\mathcal{E}_2\,\mathcal{E}_{-2}\rangle_3\ -\langle R_2\rangle_1\langle \mathcal{E}_2\,\mathcal{E}_{-2}\rangle_2\ )\ /\ \langle R_2\rangle_1^3$	$1.3(14)_{\rm stat}(28)_{\rm syst}\times 10^{-6}$	$0.01(1)_{\rm stat}(30)_{\rm syst}\times 10^{-3}$
	$(\ \langle R_2\,\mathcal{E}_3\,\mathcal{E}_{-3}\rangle_3\ -\langle R_2\rangle_1\langle \mathcal{E}_3\,\mathcal{E}_{-3}\rangle_2\ )\ /\ \langle R_2\rangle_1\langle R_3\rangle_1^2$	$-1.4(17)_{\rm stat}\times 10^{-6}$	$0.139(7)_{\rm stat}(75)_{\rm syst}\times 10^{-3}$

TABLE II. **One-, two-, and three-body properties of ^{208}Pb and ^{129}Xe inferred from the fits of LHC data.** Systematic uncertainties represent the 1σ variation of these quantities across ten samples of the posterior distributions for the nuclear density parameters. Statistical uncertainties reflect the statistical precision on the hydrodynamic events used in the design of the Bayesian fits.

collision limit we estimate

$$\frac{\kappa_{2,\rm XeXe}}{\kappa_{2,\rm PbPb}} \approx 0.95, \tag{12}$$

such that, with the values of the nuclear expectation values given in Tab. II, we obtain

$$\frac{v_2\{2\}_{\rm XeXe}}{v_2\{2\}_{\rm PbPb}} \simeq 1.72. \tag{13}$$

This result aligns nicely with the full 0-1% Trajectum calculations shown in Fig. 3 of the main text, and hence even with the experimental results. As expected, the leading-order result lies a little above the full numerical result, as it neglects corrections due to, e.g., nucleon-by-nucleon fluctuations or smearing from the finite nucleon size, which naturally counter the nuclear shape effects. For a large nucleus like ^{129}Xe, these effects are, however, small, such that we are capable of inferring the normalized two-body expectation $\langle \mathcal{E}_2\,\mathcal{E}_{-2}\rangle_2/\langle R_2\rangle_1^2$ with a robust and relatively small theoretical error.

[1] J. Weil *et al.* (SMASH), "Particle production and equilibrium properties within a new hadron transport approach for heavy-ion collisions," Phys. Rev. C **94**, 054905 (2016), arXiv:1606.06642 [nucl-th].

[2] D. Oliinychenko, V. Steinberg, J. Weil, M. Kretz, J. Staudenmaier, S. Ryu, A. Schäfer, J. Rothermel, J. Mohs, F. Li, H. E. (Petersen), L. Pang, D. Mitrovic, A. Goldschmidt, L. Geiger, J.-B. Rose, J. Hammelmann, and L. Prinz, "smash-transport/smash: Smash-1.8," (2020).

[3] G. Nijs, W. van der Schee, U. Gürsoy, and R. Snellings, "Bayesian analysis of heavy ion collisions with the heavy ion computational framework Trajectum," Phys. Rev. C **103**, 054909 (2021), arXiv:2010.15134 [nucl-th].

[4] J. S. Moreland, J. E. Bernhard, and S. A. Bass, "Alternative ansatz to wounded nucleon and binary collision scaling in high-energy nuclear collisions," Phys. Rev. C **92**, 011901 (2015), arXiv:1412.4708 [nucl-th].

[5] G. Nijs and W. van der Schee, "A generalized hydrodynamizing initial stage for Heavy Ion Collisions," (2023), arXiv:2304.06191 [nucl-th].

[6] A. Bazavov *et al.* (HotQCD), "Equation of state in (2+1)-flavor QCD," Phys. Rev. D **90**, 094503 (2014), arXiv:1407.6387 [hep-lat].

[7] J. E. Bernhard, *Bayesian parameter estimation for relativistic heavy-ion collisions*, Ph.D. thesis, Duke U. (2018), arXiv:1804.06469 [nucl-th].

[8] J. E. Bernhard, J. S. Moreland, and S. A. Bass, "Bayesian estimation of the specific shear and bulk viscosity of quark–gluon plasma," Nature Phys. **15**, 1113 (2019).

[9] S. Pratt and G. Torrieri, "Coupling Relativistic Viscous Hydrodynamics to Boltzmann Descriptions," Phys. Rev. C **82**, 044901 (2010), arXiv:1003.0413 [nucl-th].

[10] S. Acharya *et al.* (ALICE), "ALICE luminosity determination for Pb−Pb collisions at $\sqrt{s_{\rm NN}}$ = 5.02 TeV," JINST **19**, P02039 (2024), arXiv:2204.10148 [nucl-ex].

[11] J. Adam *et al.* (ALICE), "Centrality Dependence of the Charged-Particle Multiplicity Density at Midrapidity in Pb-Pb Collisions at $\sqrt{s_{\rm NN}}$ = 5.02 TeV," Phys. Rev. Lett. **116**, 222302 (2016), arXiv:1512.06104 [nucl-ex].

[12] S. Acharya *et al.* (ALICE), "Production of charged pions, kaons, and (anti-)protons in Pb-Pb and inelastic *pp* collisions at $\sqrt{s_{NN}}$ = 5.02 TeV," Phys. Rev. C **101**, 044907 (2020), arXiv:1910.07678 [nucl-ex].

[13] S. Acharya *et al.* (ALICE), "Centrality and pseudorapidity dependence of the charged-particle multiplicity density in Xe–Xe collisions at $\sqrt{s_{\rm NN}}$ =5.44TeV," Phys. Lett. B **790**, 35 (2019), arXiv:1805.04432 [nucl-ex].

[14] S. Acharya *et al.* (ALICE), "Energy dependence and fluctuations of anisotropic flow in Pb-Pb collisions at $\sqrt{s_{\rm NN}}$ = 5.02 and 2.76 TeV," JHEP **07**, 103 (2018), arXiv:1804.02944 [nucl-ex].

[15] S. Acharya *et al.* (ALICE), "Anisotropic flow in Xe-Xe collisions at $\sqrt{\mathbf{s_{NN}}} = \mathbf{5.44}$ TeV," Phys. Lett. B **784**, 82 (2018), arXiv:1805.01832 [nucl-ex].

[16] G. Aad *et al.* (ATLAS), "Correlations between flow and transverse momentum in Xe+Xe and Pb+Pb collisions at the LHC with the ATLAS detector: A probe of the heavy-ion initial state and nuclear deformation," Phys. Rev. C **107**, 054910 (2023), arXiv:2205.00039 [nucl-ex].

[17] W. D. Vousden, W. M. Farr, and I. Mandel, "Dynamic

temperature selection for parallel tempering in Markov chain Monte Carlo simulations," Mon. Not. Roy. Astron. Soc. **455**, 1919 (2016), arXiv:1501.05823.

[18] D. Foreman-Mackey, D. W. Hogg, D. Lang, and J. Goodman, "emcee: The MCMC Hammer," Publ. Astron. Soc. Pac. **125**, 306 (2013), arXiv:1202.3665 [astro-ph.IM].

[19] G. Giacalone, J. Jia, and V. Somà, "Accessing the shape of atomic nuclei with relativistic collisions of isobars," Phys. Rev. C **104**, L041903 (2021), arXiv:2102.08158 [nucl-th].

[20] G. Nijs and W. van der Schee, "Inferring nuclear structure from heavy isobar collisions using Trajectum," SciPost Phys. **15**, 041 (2023), arXiv:2112.13771 [nucl-th].

[21] H.-j. Xu, W. Zhao, H. Li, Y. Zhou, L.-W. Chen, and F. Wang, "Probing nuclear structure with mean transverse momentum in relativistic isobar collisions," Phys. Rev. C **108**, L011902 (2023), arXiv:2111.14812 [nucl-th].

[22] C. Zhang, S. Bhatta, and J. Jia, "Ratios of collective flow observables in high-energy isobar collisions are insensitive to final-state interactions," Phys. Rev. C **106**, L031901 (2022), arXiv:2206.01943 [nucl-th].

[23] H. Mäntysaari, B. Schenke, C. Shen, and W. Zhao, "Probing nuclear structure of heavy ions at energies available at the CERN Large Hadron Collider," Phys. Rev. C **110**, 054913 (2024), arXiv:2409.19064 [nucl-th].

[24] G. Giacalone *et al.*, "Nuclear Physics Confronts Relativistic Collisions Of Isobars," (2025), arXiv:2507.01454 [nucl-ex].

[25] C. Loizides, J. Kamin, and D. d'Enterria, "Improved Monte Carlo Glauber predictions at present and future nuclear colliders," Phys. Rev. C **97**, 054910 (2018), [Erratum: Phys.Rev.C 99, 019901 (2019)], arXiv:1710.07098 [nucl-ex].

[26] M. Centelles, X. Roca-Maza, X. Vinas, and M. Warda, "Origin of the neutron skin thickness of 208Pb in nuclear mean-field models," Phys. Rev. C **82**, 054314 (2010), arXiv:1010.5396 [nucl-th].

[27] B. Bally, M. Bender, G. Giacalone, and V. Somà, "Evidence of the triaxial structure of $^{\mathbf{129}}$Xe at the Large Hadron Collider," Phys. Rev. Lett. **128**, 082301 (2022), arXiv:2108.09578 [nucl-th].

[28] G. Giacalone, G. Nijs, and W. van der Schee, "Determination of the Neutron Skin of Pb208 from Ultrarelativistic Nuclear Collisions," Phys. Rev. Lett. **131**, 202302 (2023), arXiv:2305.00015 [nucl-th].

[29] G. Nijs and W. van der Schee, "Hadronic Nucleus-Nucleus Cross Section and the Nucleon Size," Phys. Rev. Lett. **129**, 232301 (2022), arXiv:2206.13522 [nucl-th].

[30] G. Giacalone, "There and Sharp Again: The Circle Journey of Nucleons and Energy Deposition," (2022), arXiv:2208.06839 [nucl-th].

[31] G. Giacalone, B. Schenke, and C. Shen, "Constraining the Nucleon Size with Relativistic Nuclear Collisions," Phys. Rev. Lett. **128**, 042301 (2022), arXiv:2111.02908 [nucl-th].

[32] F. Jonas and C. Loizides, "Centrality dependence of electroweak boson production in PbPb collisions at the CERN Large Hadron Collider," Phys. Rev. C **104**, 044905 (2021), arXiv:2104.14903 [nucl-ex].

[33] G. Pihan, A. Monnai, B. Schenke, and C. Shen, "Unveiling Baryon Charge Carriers through Charge Stopping in Isobar Collisions," Phys. Rev. Lett. **133**, 182301 (2024), arXiv:2405.19439 [nucl-th].

[34] G. Pihan, A. Monnai, B. Schenke, and C. Shen, "Neutron Skin from Conserved Charge Measurements at Collider Experiments," (2025), arXiv:2509.21644 [nucl-th].

[35] G. Pihan and V. Vovchenko, "Disentangling baryon stopping and neutron skin effects in heavy-ion collisions," (2026), arXiv:2602.04079 [hep-ph].

[36] P. Carzon, S. Rao, M. Luzum, M. Sievert, and J. Noronha-Hostler, "Possible octupole deformation of ^{208}Pb and the ultracentral v_2 to v_3 puzzle," Phys. Rev. C **102**, 054905 (2020), arXiv:2007.00780 [nucl-th].

[37] H.-j. Xu, D. Xu, S. Zhao, W. Zhao, H. Song, and F. Wang, "Investigation of an octupole breathing mode of Pb208 as a resolution to the elliptical-to-triangular azimuthal anisotropy puzzle in ultracentral relativistic heavy ion collisions," Phys. Rev. C **112**, L051901 (2025), arXiv:2504.19644 [nucl-th].

[38] L. Liu, C. Zhang, J. Chen, J. Jia, X.-G. Huang, and Y.-G. Ma, "Scaling approach to rigid and soft nuclear deformation through flow fluctuations in high-energy nuclear collisions," (2025), arXiv:2509.09376 [nucl-th].

[39] J. Auvinen, K. J. Eskola, H. Hirvonen, and H. Niemi, "Neural network enhanced Bayesian global analysis of relativistic heavy ion collisions," (2026), arXiv:2603.26413 [hep-ph].

[40] T. Duguet, G. Giacalone, S. Jeon, and A. Tichai, "Revealing the Harmonic Structure of Nuclear Two-Body Correlations in High-Energy Heavy-Ion Collisions," Phys. Rev. Lett. **135**, 182301 (2025), arXiv:2504.02481 [nucl-th].

[41] S. Bofos, B. Bally, T. Duguet, and M. Frosini, "Imaging two-body correlations in atomic nuclei via low- and high-energy processes," (2026), arXiv:2602.09890 [nucl-th].